PAPER

2D spin transport through graphene-$MnBi_2Te_4$ heterojunction

To cite this article: Xi Chen and Zheng-Zhe Lin 2022 *Nanotechnology* **33** 325201

IOP Publishing Nanotechnology
Nanotechnology 33 (2022) 325201 (9pp) https://doi.org/10.1088/1361-6528/ac6c35

2D spin transport through graphene-$MnBi_2Te_4$ heterojunction

Xi Chen and Zheng-Zhe Lin

School of Physics, Xidian University, Xi'an 710071, People's Republic of China

E-mail: zzlin@xidian.edu.cn

Received 12 March 2022, revised 22 April 2022
Accepted for publication 3 May 2022
Published 17 May 2022

Abstract

The development of two-dimensional (2D) magnetic semiconductors promotes the study of nonvolatile control of magnetoelectric nanodevices. $MnBi_2Te_4$ is the first realization of antiferromagnetic topological insulator. In semiconductor circuits, metal-semiconductor contacts are usually essential. In future all-carbon circuits, graphene is a promising material for 2D conductive connections. This work studies electronic transport through graphene-$MnBi_2Te_4$-graphene junctions. We find that graphene-$MnBi_2Te_4$ interfaces are perfect Ohmic contacts, which benefits the use of $MnBi_2Te_4$ in carbon circuits. The currents through $MnBi_2Te_4$ junctions possess high spin polarization. Compared with usual van der Waals junctions, lateral graphene-$MnBi_2Te_4$-graphene junctions present a lower barrier and much higher conductance to electrons. These findings may provide guidance for further study of 2D spin filtering.

Supplementary material for this article is available online

Keywords: 2D ferromagnetism, spin transport, heterojunction

(Some figures may appear in colour only in the online journal)

1. Introduction

The discovery of two-dimensional (2D) materials has inspired a great revolution in material science. 2D materials have been considered as building blocks for nanoelectronics and optoelectronics. In recent years, the development of 2D materials has brought new opportunities for spintronics [1–4]. Magnetic 2D materials have invoked tremendous research interest in developing magnetic nanodevices. The spin degree of freedom has been utilized to demonstrate exotic phenomena. Significant effort has been devoted to fabricating ultrathin films down to the monolayer limit because the magnetic properties of 2D layered materials change significantly as their thickness reduces to atomically thin [4, 5]. Designing conceptual magnetic devices composed of 2D magnetic monolayers may drive the development of new technology.

As basic structures for electronic devices, 2D materials can lead to drastic reduction in characteristic lengths [6–8]. As isolated atomic planes, 2D materials can be reassembled as van der Waals (vdW) heterostructures [9–11]. Different 2D materials can assemble various vdW heterostructures, which reveal new physical properties and phenomena. With distinctive electronic and optoelectronic properties, graphene- [12–15] and transition-metal-dichalcogenide-based [16–19] vdW heterostructures have attracted many research efforts. Without direct chemical bonding, vdW heterostructures are being considered as a novel way to construct devices that integrate the properties of isolated components without a transition region [20]. However, electrons across vdW heterostructures (with interlayer spacing of about 3 $\sim$ 5 Å) have to pass through a barrier. In contrast, lateral heterostructures, which are connected by covalent bonds, have close-connected atomic interfaces in the plane. A high-quality covalent interface ensures good growth characteristics and device performance of lateral heterostructures [21–23]. The development of 2D lateral heterostructures with the powerful tunability of electronic properties is of great realistic significance for next-generation device [24] and photo-chemical [25] applications. In lateral heterostructures, the connections of distinct 2D layers may be with higher transmission. Therefore, devices constituted of 2D materials with lateral arrangement are also worthy of further study.

Nonvolatile electrical control of 2D ferromagnets is proposed as a key technology for future magnetoelectric nanodevices [26]. People have found that 2D CrI_3 [27–35], $Cr_2Ge_2Te_6$ [36], $CrSiTe_3$ [37] and VSe_2 [38, 39] possess intrinsic magnetocrystalline anisotropy. 2D ferromagnetic Fe_3GeTe_2 [40–46] was found to have a Curie temperature close to room temperature (150–220 K depending on Fe occupancy [43, 44, 47]). Recently, 2D $MnBi_2Te_4$ was successfully synthesized and confirmed as an intrinsic magnetic topological insulator [48, 49]. With ferromagnetic intralayer and antiferromagnetic interlayer interactions, $MnBi_2Te_4$ was suggested to be the first realization of antiferromagnetic topological insulator [50–55]. In multi-layer $MnBi_2Te_4$, quantum phase transition can be realized by the manipulation of magnetic orientation [5, 48, 54, 55], interlayer twisting [56] or electric field [57]. Recently, $MnBi_2Te_4$ monolayer is suggested to be a material for spin transport [58]. On this basis, the construction of spintronics devices with $MnBi_2Te_4$ is worth further study.

Semiconductor devices are usually connected to external circuits. Thus, metal-semiconductor contacts are essential. In future all-carbon circuits, graphene is a promising material for 2D conductive connections. In this paper, we carry out basic study on the structure and the electronic transport through lateral and vdW graphene-$MnBi_2Te_4$-graphene junctions. Both lateral and vdW graphene-$MnBi_2Te_4$ interfaces are found to be Ohmic contacts, which benefits the use of $MnBi_2Te_4$ in carbon circuits. We design several models as the prototypes of graphene-$MnBi_2Te_4$-graphene devices. Transport calculations are performed to show the high spin polarization of currents. Lateral graphene-$MnBi_2Te_4$-graphene junctions present much higher conductance than the vdW junctions. Our findings may provide theoretical guidance for further study of spin filtering based on 2D magnetic materials.

2. Methods

We perform DFT calculations with the projector augmented wave method [59, 60], as implemented in the Vienna *ab initio* simulation package (VASP) [61–64]. Plane-wave basis set is used with a kinetic energy cutoff of 500 eV. The generalized gradient approximation of Perdew–Burke–Ernzerhof [65] plus Hubbard U correction [66] (PBE + U) is employed as the exchange-correlation functional for geometry relaxation (for obtaining the value of U, see the next paragraph). To obtain reliable results of energy bands and the projected density of states, the hybrid Heyd–Scuseria–Ernzerhof (HSE06) functional [67, 68] is employed in the electronic structure calculations. The Brillouin-zone integration is performed with a k-spacing of 0.02 $Å^{-1}$. The convergence of total energy is considered to be achieved until the total energy difference of two iterated steps is less than 10^{-5} eV. spin–orbit coupling (SOC) is included in the computation with a full k-point grid. To reduce the interlayer interactions, the replicas of the simulation system are separated by a vacuum spacing of at least 16 Å in the direction perpendicular to the 2D surface. The atomic positions are fully relaxed until the Hellmann–Feynman forces are below 0.01 eV $Å^{-1}$.

In the PBE + U approach, the rotationally invariant formalism of Hubbard U correction [66] (where only $U_{\rm eff} = U - J$ value is meaningful, the U parameter used in this paper denotes the $U_{\rm eff}$) is employed to account for the correlation energy of Mn 3d orbitals. To determine the parameter U, we adopt the linear response approach introduced by Cococcioni *et al* [69], in which the interacting (χ) and the non-interacting (χ_0) density response functions of the system with respect to localized perturbations are first calculated. Then, the parameter $U_{\rm eff} = 4.1$ eV for Mn can be obtained by $U_{\rm eff} = \chi^{-1} - \chi_0^{-1}$ (see supplementary section 1 (available online at stacks.iop.org/NANO/33/325201/mmedia) for details). To verify the reliability of the PBE + U approach, we compare the calculated energy bands at the level of PBE + U and HSE06 in supplementary section 2, showing the similarity of the two methods.

Quantum transport calculations are performed using the non-equilibrium Green's function method [70] implemented in the TRANSIESTA code [71]. The generalized gradient approximation of PBE + U is also used here. The improved Troullier–Martins pseudopotentials [72] are employed to describe the ion cores. Valence electrons are taken as C ($2s^2 2p^2$), Bi ($6s^2 6p^3$) and Te ($5s^2 5p^4$) described by double-ζ basis set, and Mn ($3d^5 4s^2$) described by double-ζ plus polarization basis set. The grid mesh cutoff is set as 350 Ry. For lateral graphene-$MnBi_2Te_4$-graphene junctions, the electrode is taken as $7 \times \sqrt{3}$ graphene electrode (x-direction: 7, z-direction: $\sqrt{3}$). For vdW graphene-$MnBi_2Te_4$-graphene junctions, the electrode is taken as $3 \times \sqrt{3}$ graphene electrode (x-direction: 3, z-direction: $\sqrt{3}$). A vacuum layer of 16 Å is set along the y direction (perpendicular to the 2D surface). For self-consistent calculations, the Brillouin zone is sampled by $9 \times 1 \times 36/21 \times 1 \times 60$ Monkhorst–Pack grid for $7 \times \sqrt{3}/3 \times \sqrt{3}$ graphene, respectively. For transmission calculations, the Brillouin zone sampling is increased to $45 \times 1 \times 180/126 \times 1 \times 240$ Monkhorst–Pack grid for $7 \times \sqrt{3}/3 \times \sqrt{3}$ graphene, respectively. The above samplings cover the graphene Dirac point. For a bias voltage V_b applied in the z-direction, the current I_σ is given by the Landauer–Büttiker formula [73]

$$I_\sigma = \frac{2e}{h}\int T_\sigma(E, V_b)\left[f_L\left(E, -, E_F, -, \frac{eV_b}{2}\right) - f_R\left(E, -, E_F, +, \frac{eV_b}{2}\right)\right]dE, \quad (1)$$

where $\sigma = \pm 1$ denotes spin up/down, $T_\sigma(E, V_b)$ is the transmission, E_F is the Fermi energy, and f_L/f_R are the Fermi–Dirac distributions of left/right electrodes at room temperature. For a 2D material width L, surface current density can be calculated as $j_\sigma = I_\sigma/L$.

3. Results and discussion

3.1. Basic properties

The primitive cell of $MnBi_2Te_4$ is hexagonal (figure 1(a)), with a lattice constant of $a_0 = 4.38$ Å and a magnetic moment of $m = 5.0\ \mu_B$. The Mn atomic layer is sandwiched between

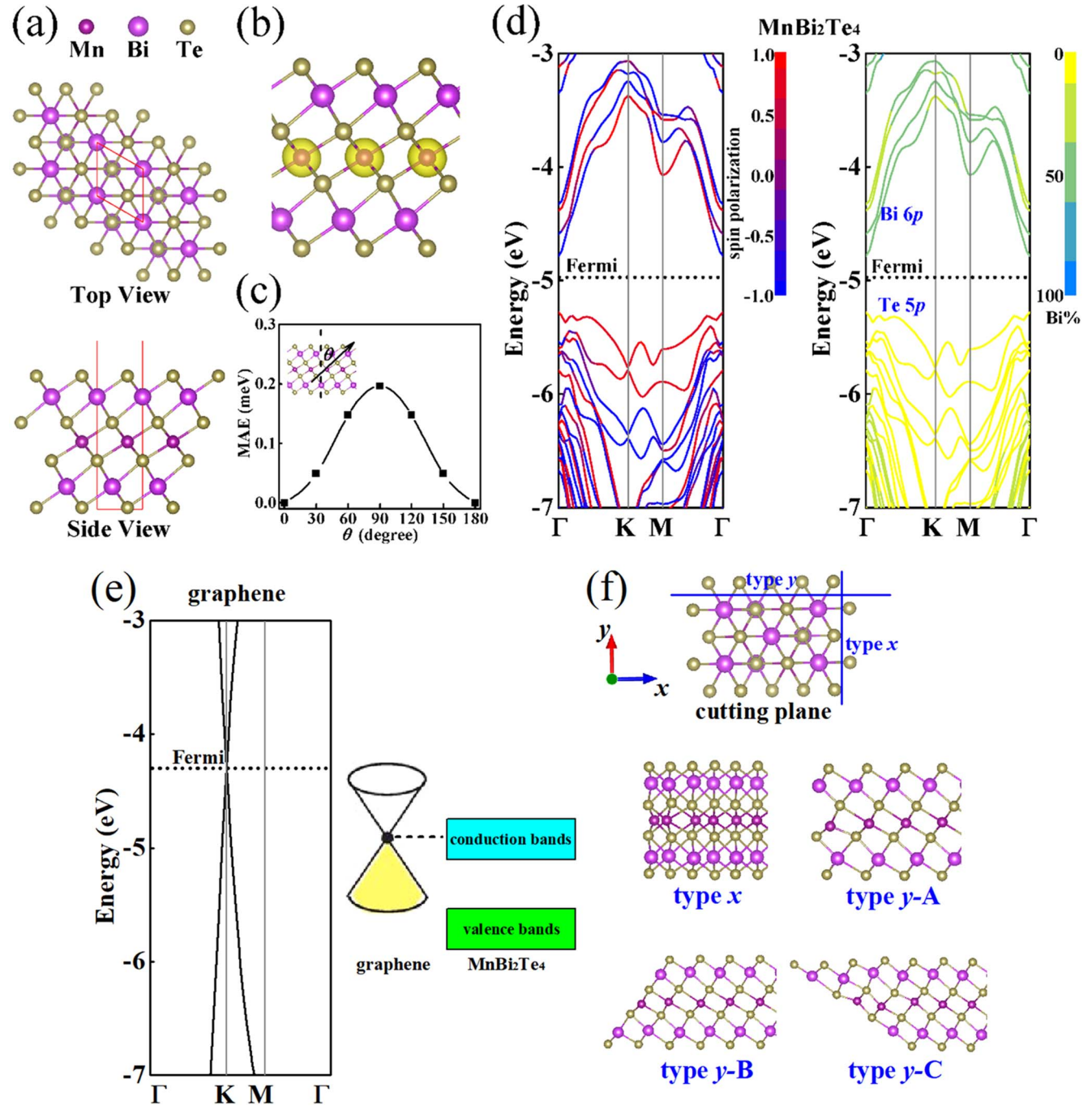

Figure 1. (a) Structure of $MnBi_2Te_4$. The primitive cell is shown by red lines. (b) The isosurface of spin density difference in $MnBi_2Te_4$ with a value of $\rho_\uparrow$ - $\rho_\downarrow$=0.01 e Å^{-3}. (c) MAE varying with angle θ that is the angle relative to the direction perpendicular to $MnBi_2Te_4$ surface. Energy bands of (d) $MnBi_2Te_4$ (shown by spin-polarization and Bi-orbital-proportion resolved) and (e) graphene are plotted with the vacuum level set to zero. (f) Four types of $MnBi_2Te_4$ edges along x and y directions. The cutting planes are shown in blue lines.

two Te–Bi–Te slabs. The magnetic coupling between Mn^{2+} is transmitted by indirect exchange of Te. The magnetic moments are mainly distributed on Mn^{2+} ($3d^5$) whose atomic spin is $S = 5/2$. To understand the distribution of magnetic moments, spin density difference, i.e. the difference $\rho_\uparrow$ - $\rho_\downarrow$ of the spin-up and spin-down electron density, is plotted in figure 1(b). The region of spin polarization further indicates the magnetic moments around Mn atoms. Magnetic anisotropy energy (MAE) (figure 1(c)) indicates that the easy axis is perpendicular to $MnBi_2Te_4$ surface.

Table 1. Formation energies of the edges in $MnBi_2Te_4$.

Formation Energy (meV Å^{-2})			
x	y-A	y-B	y-C
28.8	35.9	22.7	62.2

The energy bands of $MnBi_2Te_4$ are plotted in figure 1(d). Within SOC, an electron in a certain state does not have a definite spin. The electronic wavefunction is presented as $\Psi = (\Psi_\uparrow(\mathbf{r}), \Psi_\downarrow(\mathbf{r}))^T$, and the spin polarization of a state reads

$$P = \frac{\int|\Psi_\uparrow(\mathbf{r})|^2 d^3\mathbf{r} - \int|\Psi_\downarrow(\mathbf{r})|^2 d^3\mathbf{r}}{\int|\Psi_\uparrow(\mathbf{r})|^2 d^3\mathbf{r} + \int|\Psi_\downarrow(\mathbf{r})|^2 d^3\mathbf{r}}. \quad (2)$$

Thus, we plot each band state with color to show the polarization. On the left panel of figure 1(d), we can see the spin-up valence band top and the spin-down conduction band bottom. The valence and conduction bands are mainly composed of Bi 6p and Te 5p orbitals. To plot orbital constituents of the band states, the contributions of Bi 6p and Te 5p orbitals on state $|\ \Psi >$ are expressed as $|<\text{Bi } 6p\ |\ \Psi>|^2$ and $|<\text{Te } 5p\ |\ \Psi>|^2$, respectively. Then, the orbital proportion of $|\ \Psi >$ reads

$$\text{Bi\%} = \frac{|<\text{Bi } 6p|\Psi>|^2}{|<\text{Bi } 6p|\Psi>|^2 + |<\text{Te } 5p|\Psi>|^2}. \quad (3)$$

On the right panel of figure 1(d), we can see that the valence bands are mainly composed of Te 5p orbitals, while the conduction bands are mainly composed of Bi 6p orbitals.

To investigate the band alignment in the graphene-$MnBi_2Te_4$ junction, the energy bands of $MnBi_2Te_4$ (figure 1(d)) and graphene (figure 1(e)) are plotted with the vacuum level set to zero. The Dirac cone of graphene ($E_F = -4.29$ eV) is higher than the Fermi level ($E_F = -4.97$ eV) and even the conduction band bottom ($E_{CBM} = -4.78$ eV) of $MnBi_2Te_4$. So, the graphene-$MnBi_2Te_4$ junction will be metal-semiconductor contact with electrons injected from graphene to $MnBi_2Te_4$, i.e. an Ohmic contact. The details are discussed in section 3.2.

For the follow-up study of graphene-$MnBi_2Te_4$ contact, the edge types of $MnBi_2Te_4$ are investigated here. We consider cutting $MnBi_2Te_4$ along natural cleavage planes, i.e. the atoms on the cut surface are basically in a plane. Figure 1(f) shows four types of relaxed edges, among which type ***x*** is cut along the y direction, and type ***y*-A**, ***y*-B**, ***y*-C** are cut along the x direction. The edge stability is represented by the formation energy

$$E_{edge} = (E_{cleaved} - E_{bulk})/2S, \quad (4)$$

in which S is the surface area of the cutting plane (one cutting produces two surfaces). Table 1 lists the formation energies. We can see that type ***y*-B** with the lowest edge formation energy is the most stable. In the following text, we mainly consider the contact of the ***y*-B** edge with graphene.

3.2. Lateral graphene-$MnBi_2Te_4$ junction

In this section, we consider the properties of lateral graphene-$MnBi_2Te_4$ junctions. For graphene, the zigzag edge has a smoother arrangement of atoms than the armchair edge, and it is more stable than the armchair edge [74]. So, we focus on the contact of zigzag graphene edge with the most stable ***y*-B** $MnBi_2Te_4$ edge. The C–C bond length in graphene is 1.42 Å. Along the zigzag direction of graphene, the periodic distance is $1.42 \times\sqrt{3} = 2.46$ Å. In comparison, the periodic distance along the x direction of $MnBi_2Te_4$ is $a_0 = 4.38$ Å. The best lattice match of zigzag graphene and ***y*-B** $MnBi_2Te_4$ edges is 7:4 with a periodic length of 17.37 Å (for graphene, $2.46 \times 7 = 17.22$ Å; for $MnBi_2Te_4$, $4.38 \times 4 = 17.52$ Å; taking their average 17.37 Å with a $\pm 0.9\%$ compromise for both graphene and $MnBi_2Te_4$). It is worth noting that lattice match is important to the stability of the connection. All the type ***y*** edges of $MnBi_2Te_4$ have a periodic width $a_0 = 4.38$ Å, while that of type ***x*** edge is 7.57 Å. For edge ***x***, the best match is one period of edge ***x*** connecting to three periods of graphene zigzag edge ($2.46 \times 3 = 7.38$ Å), for which a $\pm 1.2\%$ compromise is need. So, each type of $MnBi_2Te_4$ edge can found a good match with graphene. The match of type ***y*** is slightly better than type ***x***. Considering type ***y*-B** is the most stable $MnBi_2Te_4$ edge, in the following we study the electron transport through graphene-$MnBi_2Te_4$(type ***y*-B**)-graphene systems.

We consider two types of contacts. The first one is contact type **LA** with graphene connected to the bottom layer of $MnBi_2Te_4$ (figure 2(a)). The second one is contact type **LB** with graphene connected to the middle of $MnBi_2Te_4$ (figure 2(b)). To find the most stable graphene-$MnBi_2Te_4$ connection, energy profile with different alignment is calculated for each type of contact (see the right panels of figures 2(a) and (b)). We start from one C atom aligned with one Te atom as 0% displacement. When the C atom is aligned with the next Te atom, the displacement is defined as 100%. In contact type **LA**, C–Te bonding exists. With increasing slip, old C–Te bonds break and new C–Te bonds form. The fluctuation in the energy profile is small (less than 0.03 eV). In contact type **LB**, C–Te bonding pulls on the surrounding Bi and Mn atoms, leading to complex contact structure. Thus, the fluctuation in the energy profile is large ($\sim$1.0 eV). The most stable configuration is located at a displacement of 25%. In the following text, we only study the most stable configurations of contact **LA** and **LB**.

In order to investigate the spatial distribution of electron states in lateral graphene-$MnBi_2Te_4$ junction, local density of states (LDOS)

$$n(\varepsilon, \mathbf{r}, \sigma) = \sum_{i\mathbf{k}} |\Psi_{i\mathbf{k}\sigma}(\mathbf{r})|^2 \delta(\varepsilon - \varepsilon_{i\mathbf{k}\sigma}), \quad (5)$$

is calculated throughout the junction. Here, ε is the energy. $\mathbf{r}$ is a position. σ denotes the spin. $\Psi_{i\mathbf{k}\sigma}$ is the ith state on Bloch wave vector $\mathbf{k}$ and spin σ. To present the state distribution along the lateral z-direction, xy-integrated LDOS

$$n_l(\varepsilon, z) = \int n(\varepsilon, \mathbf{r}, \sigma) dxdy, \quad (6)$$

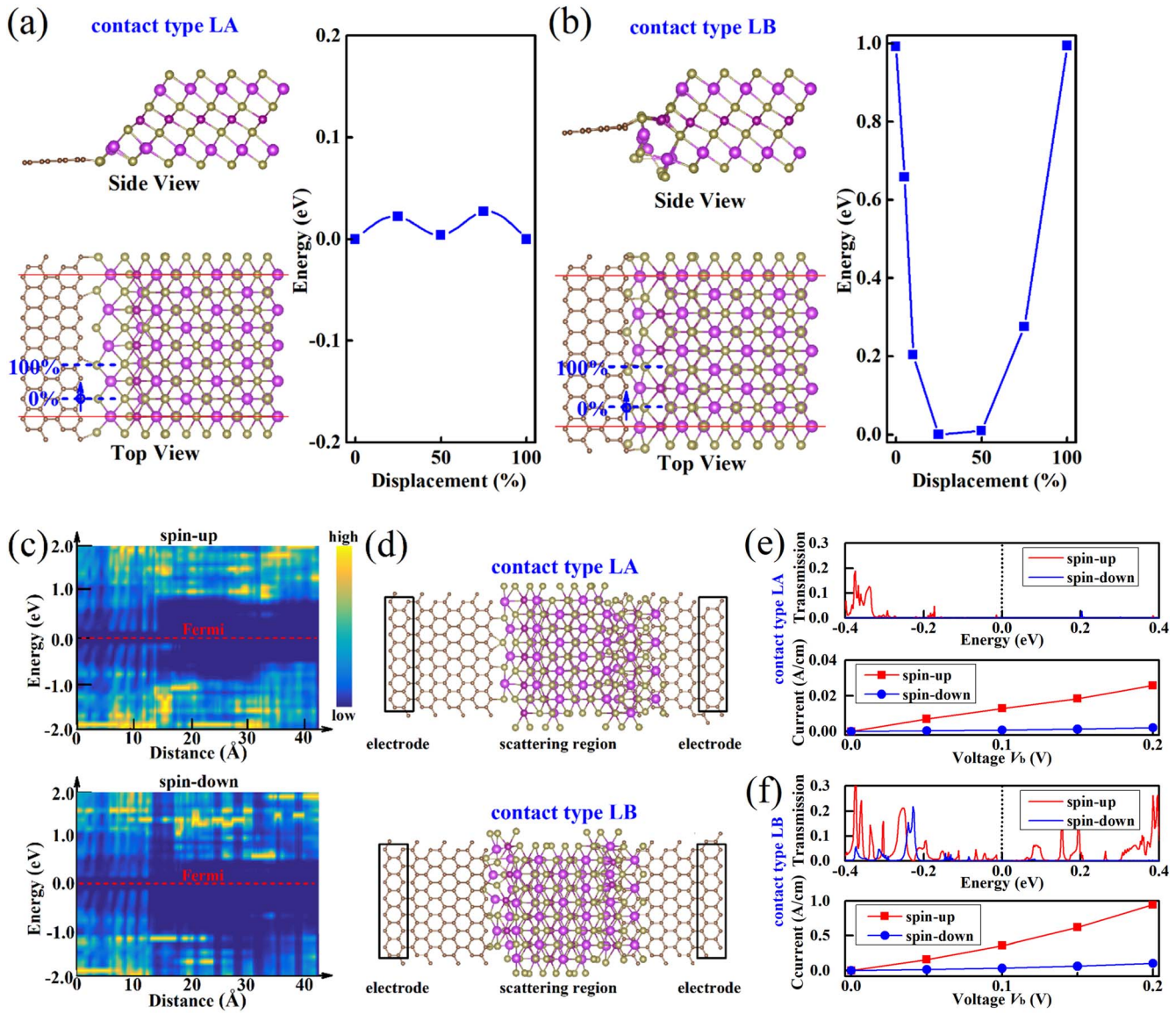

Figure 2. Type (a) LA and (b) LB of lateral graphene-$MnBi_2Te_4$ contacts. The alignment is quantified by the displacement of a C atom relative to a Te atom. The energy profiles changing with displacement are shown. (c) *xy*-integrated LDOS of the electron transmission (in arb. unit) through contact type LB. (d) Two-probe graphene-$MnBi_2Te_4$-graphene configurations with contact type LA and LB, whose transmission spectra and current–voltage curves are shown in (e) and (f), respectively.

is calculated. As an example, the calculation result of contact type **LB** is shown in figure 2(c). In the graphene side (left), the semimetallic property (i.e. the Dirac-cone bands) makes the $n_l(\varepsilon, z)$ above and below the Fermi level contact to each other (at Fermi level, $n_l(\varepsilon, z) = 0$). At the $MnBi_2Te_4$ side, band gaps exist for both spin-up and spin-down cases. With electron injection from graphene to $MnBi_2Te_4$, their Fermi energies are pulled to the same level. No obvious band bending is found near the connection place. At the $MnBi_2Te_4$ side, the spin-down conduction band is lower than the spin-up one (like the bulk bands figure 1(d)).

To study the spin transport through lateral graphene-$MnBi_2Te_4$ contact, we construct two-probe graphene-$MnBi_2Te_4$-graphene models of contact types **LA** and **LB** with $\sqrt{3} \times 7$ graphene electrodes and two buffer layers in both left and right sides (figure 2(d)). The transmission spectra and current–voltage curves are shown in figures 2(e) and (f). We can see that the currents through contacts **LA** and **LB** are highly spin-polarized. In contact type **LA**, the spin polarization of current is 89%–85% in the range of $V_b = 0$–0.2 V. In contact type **LB**, the spin polarization of current is 83%–80% in the range of $V_b = 0$–0.2 V. In contact type **LB**, graphene is connected to the middle of $MnBi_2Te_4$, and thus electrons pass through more easily than they do through $MnBi_2Te_4$ surface. Under a same bias voltage, the current through **LB** is about forty times as much as that of **LA**. Both **LA** and **LB** contacts show a feature of Ohmic contact with the nearly linear

current–voltage curves. The difference of transmission between **LA** and **LB** can be understood by the electron distribution of $MnBi_2Te_4$ conduction band. Supplementary figure S4(a) shows the Bloch function of $MnBi_2Te_4$ conduction band minimum, in which we can see that it mainly composed of Bi 6*p* states and parts of the 5*p* states of the inner Te layers. $MnBi_2Te_4$ has two Bi atomic layers. In contact **LA**, graphene only connects to one Bi layer, and thus the transmission is low. Supplementary figure S4(b) shows the detail of transmission spectrum of **LA**. In contact **LB**, graphene connects to both Bi layers and the inner Te layers. Thus it obtains higher transmission. We also consider other types of graphene-$MnBi_2Te_4$-graphene junctions. Supplementary section 6 presents the transport through a junction in which the graphene zigzag edge is connected to the type ***x*** $MnBi_2Te_4$ edge. The current through the junction also shows spin polarization. The spin transport through graphene-$MnBi_2Te_4$-graphene junctions is general, independent of the type of $MnBi_2Te_4$ edge.

3.3. vdW graphene-$MnBi_2Te_4$ junction

vdW heterojunctions are an emerging kind of device structure, in which 2D atomic layers are stacked to realize expected functions by the combination. In this section, electronic transport through graphene-$MnBi_2Te_4$ vdW heterostructures is studied to make comparison with the lateral junctions. Our calculation model matches $\sqrt{3} \times \sqrt{3}$ graphene (lattice vector length 4.26 Å) with 1×1 $MnBi_2Te_4$ lattice (lattice vector length 4.38 Å) and takes an average lattice vector length 4.32 Å, with a ±1% compromise for both graphene and $MnBi_2Te_4$. We consider hollow, top and bridge types of stacking (figure 3(a)). Binding energy

$$E_b = (E_{hetero} - E_{graphene} - E_{MnBi_2Te_4})/S, \tag{7}$$

is used to evaluate the stability of difference stacking (S is the surface area). Table 2 lists the calculation results, indicating that hollow stacking is the most stable (which is used in the following simulations). The balance distance from graphene layer to $MnBi_2Te_4$ surface is 3.58 Å.

The spin-resolved energy bands of hollow-type graphene-$MnBi_2Te_4$ heterostructure are plotted in the left panel of figure 3(b) (spin polarization calculated by equation (2)). The Fermi energy respective to the vacuum level is −4.62 eV, which is between that of isolated graphene and $MnBi_2Te_4$. To resolve the energy bands distribution, orbital contribution of graphene and $MnBi_2Te_4$ in every Bloch state is calculated, and the proportion of $MnBi_2Te_4$ is evaluated by the method similar to equation (3). In the right panel of figure 3(b), we can see that graphene and $MnBi_2Te_4$ keep their original band structures. vdW interaction just combines the two 2D layers, but does not strongly affects the band structure.

In vdW heterostructures, the two 2D layers do not closely contact to each other. For electronic transport, a barrier exists in the space between the two layers. To reveal the barrier shape, average Hartree potential

$$\bar{V}_H(z) = \frac{1}{S}\int V_H(\mathbf{r})dxdy, \tag{8}$$

is calculated along the z-direction perpendicular to the 2D surfaces. Here $V_H(\mathbf{r})$ is the Hartree potential at position $\mathbf{r}$. Equation (8) takes the average in the *xy* plane. In figure 3(c), we pay attention to the part of $\bar{V}_H$ above the Fermi energy. A tunneling potential barrier $\Phi_{TB} = 4.19$ eV impedes electron transport through the graphene-$MnBi_2Te_4$ interface. Φ_{TB} and the barrier width $d_{TB} = 1.93$ Å determine the transmission. Based on Simmons tunneling injection model [75, 76], the tunneling-specific resistivity across the interface can be estimated as

$$\rho \approx \frac{4\pi^2\hbar d_{TB}^2}{e^2}\frac{\exp\left(\frac{(2m)^{1/2}}{\hbar}d_{TB}\Phi_{TB}\right)}{\frac{(2m)^{1/2}}{\hbar}d_{TB}\Phi_{TB} - 1}, \tag{9}$$

where m is the electron mass. The calculated resistivity $\rho \approx 1.5 \times 10^{-9}$ Ω·cm^2 is comparable to that of the recently reported Bi/MoS_2 contact of ultralow contact resistance [77].

Then, we study the spin transport through two-probe vdW graphene-$MnBi_2Te_4$-graphene junctions. Two types of structures are considered. The first type **HA** is composed of a $MnBi_2Te_4$ slab sandwiched between two graphene layers (figure 3(d)). The second type **HB** is composed of a $MnBi_2Te_4$ slab suspended on two graphene layers (figure 3(f)). The transmission spectra and current–voltage curves of **HA** and **HB** are shown in figures 3(e) and (g), respectively. Due to the scattering caused by vacuum barrier tunneling, the transmission and currents are much smaller than those in the lateral two-probe junctions (figures 2(e) and (f)). The **HB** type has a horizontal structure that benefits electron flows with lower scattering. So, under same bias voltage, the current through **HB** is about ten times as much as that **HA**. In the **HA** junction, currents through $MnBi_2Te_4$ have a spin polarization of 98%–94% in the range of $V_b = 0$–0.2 V. In the **HB** junction, the spin polarization of currents is 94%–71% in the range of $V_b = 0$–0.2 V. Overall, in both lateral and vdW junctions, as long as the current goes through the Mn layer, high spin polarization can be realized. In contrast, such spin transport cannot be realized in usual $MnBi_2Te_4$ junction structures. As an example, supplementary section 3 shows the electronic transmission and currents through Cu-$MnBi_2Te_4$-Cu junction. The contact is also Ohmic. But the spin polarization is only about 37%. To understand the spin polarization in metal-$MnBi_2Te_4$-metal junctions, the energy band diagram of the Cu-$MnBi_2Te_4$-Cu system is analyzed in supplementary section 5. In figure S5(b), we can see that in the Cu-$MnBi_2Te_4$-Cu junction, the main part of $MnBi_2Te_4$ bands are contaminated by Cu-bulk

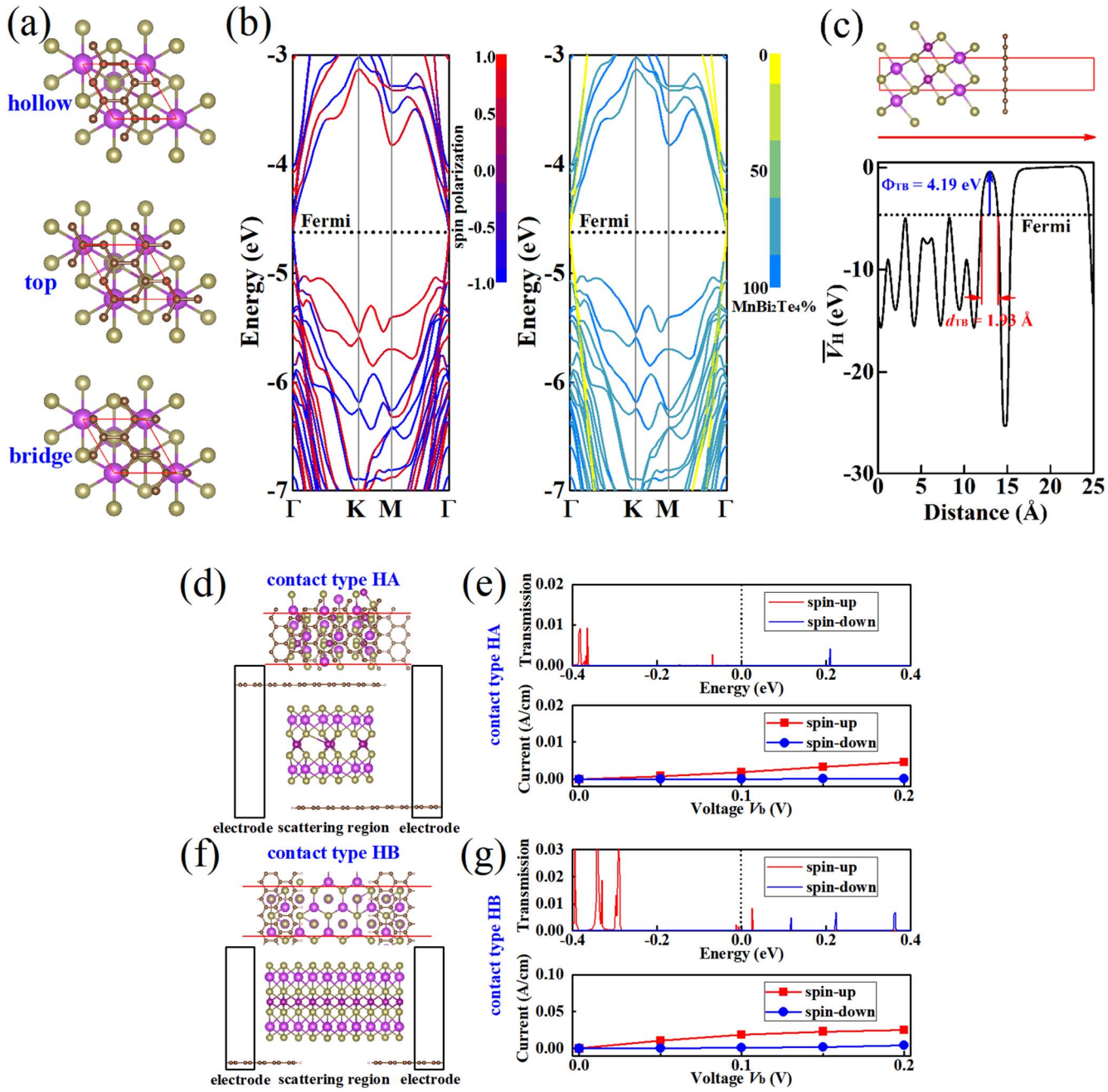

Figure 3. (a) Structures of graphene-$MnBi_2Te_4$ vdW heterostructures. (b) Energy bands of hollow-type graphene-$MnBi_2Te_4$ vdW heterostructure, shown by spin-polarization and $MnBi_2Te_4$-orbital-proportion resolved. The vacuum level set to zero. (c) Average Hartree potential $\bar{V}_H$ in the hollow-type graphene-$MnBi_2Te_4$ vdW heterostructure. (d) Structure, (e) transmission spectrum and current–voltage curve of vertically stacked HA type of graphene-$MnBi_2Te_4$ vdW heterostructure. (f) Structure, (g) transmission spectrum and current–voltage curve of horizontally stacked HB type of graphene-$MnBi_2Te_4$ vdW heterostructure.

Table 2. Binding energies of graphene-$MnBi_2Te_4$ vdW heterostructures.

Binding Energy (meV Å^{-2})		
Hollow	Top	Bridge
−16.0	−15.4	−15.5

bands. The Cu electrodes are spin-unpolarized. The extend states of Cu-bulk Bloch waves through $MnBi_2Te_4$ weaken the spin polarization of current. In contrast, graphene is a Dirac material with vanishing density of states at the Dirac point. So, graphene has very little effect on the energy bands of $MnBi_2Te_4$. This reason leads to high spin polarization in lateral and vdW graphene-$MnBi_2Te_4$-graphene junctions.

4. Conclusions

In conclusion, the spin transport through graphene-$MnBi_2Te_4$-graphene junctions are studied by employing DFT calculations. The results prove that the graphene-$MnBi_2Te_4$ connections are Ohmic contacts. The resistance of vdW graphene-$MnBi_2Te_4$ connections is close to that of the recently reported Bi/MoS_2 contact of ultralow contact resistance. By contrast, lateral graphene-$MnBi_2Te_4$ connections are more favorable for electrons to pass through. Much higher currents can be realized by lateral graphene-$MnBi_2Te_4$ connections. In both lateral and vdW graphene-$MnBi_2Te_4$ junctions, high spin polarization can be obtained. Our work may provide useful theoretical guidance for exploring new spintronic devices based on 2D vdW magnetic materials.

Acknowledgments

This work is supported by the Natural Science Basic Research Program of Shaanxi Province (Nos. 2021JM-117 & 2021JQ-185), the Fundamental Research Funds for the Central Universities (No. XJS200503), and the Postdoctoral Research Project of Shaanxi Province (No. 2018BSHEDZZ68). All authors would like to acknowledge the computing facilities at High Performance Computing Center of Xidian University.

Data availability statement

All data that support the findings of this study are included within the article (and any supplementary files).

Conflict of interest

The authors declare that they have no conflict of interest.

ORCID iDs

Xi Chen https://orcid.org/0000-0001-6321-2279
Zheng-Zhe Lin https://orcid.org/0000-0001-7188-6257

References

[1] Gibertini M, Koperski M, Morpurgo A F and Novoselov K S 2019 Magnetic 2D materials and heterostructures *Nat. Nanotech.* **14** 408
[2] Thiel L *et al* 2019 Probing magnetism in 2D materials at the nanoscale with single-spin microscopy *Science* **364** 973
[3] Cardoso C, Soriano D, Garcia-Martinez N A and Fernandez-Rossier J 2018 Van der Waals spin valves *Phys. Rev. Lett.* **121** 067701
[4] Gong S-J 2018 Electrically induced 2D half-metallic antiferromagnets and spin field effect transistors *Proc. Natl. Acad. Sci. USA* **115** 8511
[5] Deng Y *et al* 2020 Quantum anomalous hall effect in intrinsic magnetic topological insulator $MnBi_2Te_4$ *Science* **367** 895
[6] Butler S Z *et al* 2013 Progress, challenges, and opportunities in two-dimensional materials beyond graphene *ACS Nano* **7** 2898
[7] Hamm J M and Hess O 2013 Two two-dimensional materials are better than one *Science* **340** 1298
[8] Koski K J and Cui Y 2013 The new skinny in two-dimensional nanomaterials *ACS Nano* **7** 3739
[9] Britnell L *et al* 2012 Field-effect tunneling transistor based on vertical graphene heterostructures *Science* **335** 947
[10] Geim A K and Grigorieva I V 2013 Van der Waals heterostructures *Nature* **499** 419
[11] Balu R, Zhong X L, Pandey R and Karna S P 2012 Effect of electric field on the band structure of graphene/boron nitride and boron nitride/boron nitride bilayers *Appl. Phys. Lett.* **100** 3
[12] Li W *et al* 2017 Tuning the Schottky barrier in the arsenene/graphene van der Waals heterostructures by electric field *Physica* E **88** 6
[13] Padilha J E, Fazzio A and da Silva A J R 2015 van der Waals Heterostructure of phosphorene and graphene: tuning the schottky barrier and doping by electrostatic gating *Phys. Rev. Lett.* **114** 066803
[14] Zhang F, Li W and Dai X 2016 Effects of interlayer coupling on the electronic structures of antimonene/graphene van der Waals heterostructures *Superlattices Microst.* **100** 826
[15] Jun L *et al* 2014 Photoinduced doping in heterostructures of graphene and boron nitride *Nat. Nanotech.* **9** 348
[16] Komsa H-P and Krasheninnikov A V 2013 Electronic structures and optical properties of realistic transition metal dichalcogenide heterostructures from first principles *Phys. Rev.* B **88** 085318
[17] Liu X and Li Z 2015 Electric field and strain effect on graphene-MoS_2 hybrid structure: *ab initio* calculations *J. Phys. Chem. Lett.* **6** 3269
[18] Fang H *et al* 2014 Strong interlayer coupling in van der Waals heterostructures built from single-layer chalcogenides *Proc. Natl. Acad. Sci. USA* **111** 6198
[19] Latini S, Winther K T, Olsen T and Thygesen K S 2017 Interlayer excitons and band alignment in $MoS_2/hBN/WSe_2$ van der Waals heterostructures *Nano Lett.* **17** 938
[20] Yan Z-Z, Jiang Z-H, Lu J-P and Ni Z-H 2018 Interfacial charge transfer in WS_2 monolayer/$CsPbBr_3$ microplate heterostructure *Front. Phys.* **13** 138115
[21] Pizzocchero F *et al* 2016 The hot pick-up technique for batch assembly of van der Waals heterostructures *Nat. Commun.* **7** 11894
[22] Liu L *et al* 2014 Lateral heterojunctions within monolayer $MoSe_2$–WSe_2 semiconductors *Science* **343** 163
[23] Levendorf M P *et al* 2012 Graphene and boron nitride lateral heterostructures for atomically thin circuitry *Nature* **488** 627
[24] Wang J, Li Z, Chen H, Deng G and Niu X 2019 Recent Advances in 2D Lateral Heterostructures *Nano-Micro Lett.* **11** 48
[25] Hou J *et al* 2017 Atomically thin mesoporous In_2O_3-x/In_2S_3 lateral heterostructures enabling robust broadband-light photo-electrochemical water splitting *Adv. Energy Mat.* **8** 1701114
[26] Zhao Y, Zhang J-J, Yuan S and Chen Z 2019 Nonvolatile electrical control and heterointerface-induced half-metallicity of 2D ferromagnets *Adv. Func. Mat.* **29** 1901420
[27] Jiang P *et al* 2019 Stacking tunable interlayer magnetism in bilayer CrI_3 *Phys. Rev.* B **99** 144401
[28] Kim H H *et al* 2018 One million percent tunnel magnetoresistance in a magnetic van der Waals Heterostructure *Nano Lett.* **18** 4885

[29] Song T *et al* 2018 Giant tunneling magnetoresistance in spin-filter van der Waals heterostructures *Science* **360** 1214
[30] Wang Z *et al* 2018 Very large tunneling magnetoresistance in layered magnetic semiconductor CrI_3 *Nat. Comm.* **9** 2516
[31] Sivadas N, Okamoto S, Xu X, Fennie C J and Xiao D 2018 Stacking-dependent magnetism in bilayer CrI_3 *Nano Lett.* **18** 7658
[32] Jian P H, Li L, Liao Z L, Zhao Y X and Zhong Z C 2018 Spin direction-controlled electronic band structure in two-dimensional ferromagnetic CrI3 *Nano Lett.* **18** 3844
[33] Jin W *et al* 2018 Raman fingerprint of two terahertz spin wave branches in a two-dimensional honeycomb Ising ferromagnet *Nature Comm.* **9** 5122
[34] Kim H H *et al* 2019 Tailored tunnel magnetoresistance response in three ultrathin chromium trihalides *Nano Lett.* **19** 5739
[35] Song T *et al* 2019 Voltage control of a van der Waals spin-filter magnetic tunnel junction *Nano Lett.* **19** 915
[36] Gong C *et al* 2017 Discovery of intrinsic ferromagnetism in two-dimensional van der Waals crystals *Nature* **546** 265
[37] Zhang J *et al* 2019 Unveiling electronic correlation and the ferromagnetic superexchange mechanism in the van der Waals crystal $CrSiTe_3$ *Phys. Rev. Lett.* **123** 047203
[38] Bonilla M *et al* 2018 Strong room-temperature ferromagnetism in VSe_2 monolayers on van der Waals substrates *Nat. Nanotechnol.* **13** 289
[39] Pan L *et al* 2019 Two-dimensional XSe_2 (X = Mn, V) based magnetic tunneling junctions with high Curie temperature *Chin. Phys.* B **28** 107504
[40] Deng Y *et al* 2018 Gate-tunable room-temperature ferromagnetism in two-dimensional Fe_3GeTe_2 *Nature* **563** 94
[41] Wang Z, Sapkota D, Taniguchi T, Watanabe K, Mandrus D and Morpurgo A F 2018 Tunneling spin valves based on Fe3GeTe2/hBN/Fe3GeTe2 van der Waals heterostructures *Nano Lett.* **18** 4303
[42] Chen B *et al* 2013 Magnetic properties of layered itinerant electron ferromagnet Fe_3GeTe_2 *J. Phys. Soc. Jap.* **82** 124711
[43] Deiseroth H J, Aleksandrov K, Reiner C, Kienle L and Kremer R K 2006 Fe_3GeTe_2 and Ni_3GeTe_2—two new layered transition-metal compounds: crystal structures, HRTEM investigations, and magnetic and electrical properties *Eur. J. Inorg. Chem.* **1561** 1561–7
[44] May A F, Calder S, Cantoni C, Cao H and McGuire M A 2016 Magnetic structure and phase stability of the van der Waals bonded ferromagnet $Fe_{3-x}GeTe_2$ *Phys. Rev.* B **93** 014411
[45] Tian C K *et al* 2019 Domain wall pinning and hard magnetic phase in Co-doped bulk single crystalline Fe3GeTe2 *Phys. Rev.* B **99** 6
[46] Fei Z Y *et al* 2018 Two-dimensional itinerant ferromagnetism in atomically thin Fe_3GeTe_2 *Nature Mater.* **17** 778
[47] Liu S *et al* 2017 Wafer-scale two-dimensional ferromagnetic Fe_3GeTe_2 thin films grown by molecular beam epitaxy *npj 2D Mater. Appl.* **1** 30
[48] Li J *et al* 2019 Intrinsic magnetic topological insulators in van der Waals layered $MnBi_2Te_4$-family materials *Sci. Adv.* **5** eaaw5685
[49] Gong Y *et al* 2019 Experimental realization of an intrinsic magnetic topological insulator *Chin. Phys. Lett.* **36** 076801
[50] Eremeev S V, Otrokov M M and Chulkov E V 2017 Competing rhombohedral and monoclinic crystal structures in $MnPn_2Ch_4$ compounds: an *ab-initio* study *J. Alloys Compd.* **709** 172
[51] Zhang D, Shi M, Zhu T, Xing D, Zhang H and Wang J 2019 Topological axion states in the magnetic insulator $MnBi_2Te_4$ with the quantized magnetoelectric effect *Phys. Rev. Lett.* **122** 206401
[52] Otrokov M M *et al* 2019 Prediction and observation of an antiferromagnetic topological insulator *Nature* **576** 416
[53] Otrokov M M *et al* 2019 Unique thickness-dependent properties of the van der Waals interlayer antiferromagnet $MnBi_2Te_4$ films *Phys. Rev. Lett.* **122** 107202
[54] Li J, Wang C, Zhang Z, Gu B-L, Duan W and Xu Y 2019 Magnetically controllable topological quantum phase transitions in the antiferromagnetic topological insulator $MnBi_2Te_4$ *Phys. Rev.* B **100** 121103(R)
[55] Li B *et al* 2020 Competing magnetic interactions in the antiferromagnetic topological insulator $MnBi_2Te_4$ *Phys. Rev. Lett.* **124** 167204
[56] Lian B, Liu Z, Zhang Y and Wang J 2020 Flat chern band from twisted bilayer $MnBi_2Te_4$ *Phys. Rev. Lett.* **124** 126402
[57] You J-Y, Dong X-J, Gu B and Su G 2021 Electric field induced topological phase transition and large enhancements of spin–orbit coupling and Curie temperature in two-dimensional ferromagnetic semiconductors *Phys. Rev.* B **103** 104403
[58] An Y *et al* 2021 Nanodevices engineering and spin transport properties of $MnBi_2Te_4$ monolayer *npj Comp. Mat.* **7** 45
[59] Kresse G and Joubert D 1999 From ultrasoft pseudopotentials to the projector augmented-wave method *Phys. Rev.* B **59** 1758
[60] Blöchl P E 1994 Projector augmented-wave method *Phys. Rev.* B **50** 17953
[61] Kresse G and Furthmüller J 1996 Efficient iterative schemes for *ab initio* total-energy calculations using a plane-wave basis set *Phys. Rev.* B **54** 11169
[62] Kresse G and Furthmüller J 1996 Efficiency of *ab-initio* total energy calculations for metals and semiconductors using a planewave basis set *Comp. Mater. Sci.* **6** 15
[63] Kresse G and Hafner J 1993 *Ab initio* molecular dynamics for liquid metals *Phys. Rev.* B **47** 558
[64] Kresse G and Hafner J 1994 *Ab initio* molecular-dynamics simulation of the liquid-metal–amorphous-semiconductor transition in germanium *Phys. Rev.* B **49** 14251
[65] Perdew J P, Burke K and Ernzerhof M 1996 Generalized gradient approximation made simple *Phys. Rev. Lett.* **77** 3865
[66] Dudarev S L, Botton G A, Savrasov S Y, Humphreys C J and Sutton A P 1998 Electron-energy-loss spectra and the structural stability of nickel oxide: an LSDA + U study *Phys. Rev.* B **57** 1505
[67] Heyd J, Scuseria G E and Ernzerhof M 2003 Hybrid functionals based on a screened Coulomb potential *J. Chem. Phys.* **118** 8207–15
[68] Heyd J, Scuseria G E and Ernzerhof M 2006 Erratum: 'Hybrid functionals based on a screened Coulomb potential' *J. Chem. Phys.* **124** 219906
[69] Cococcioni M and de Gironcoli S 2005 Linear response approach to the calculation of the effective interaction parameters in the LDA + U method *Phys. Rev.* B **71** 035105
[70] Taylor J, Guo H and Wang J 2001 *Ab initio* modeling of quantum transport properties of molecular electronic devices *Phys. Rev.* B **63** 245407
[71] Brandbyge M, Mozos J L, Ordejón P, Taylor J and Stokbro K 2002 Density-functional method for nonequilibrium electron transport *Phys. Rev.* B **65** 165401
[72] Troullier N and Martins J L 1991 Efficient pseudopotentials for plane-wave calculations *Phys. Rev.* B **43** 1993
[73] Büttiker M, Imry Y, Landauer R and Pinhas S 1985 Generalized many-channel conductance formula with application to small rings *Phys. Rev.* B **31** 6207
[74] Acik M and Chabal Y J 2011 Nature of graphene edges: a review *Jpn. J. Appl. Phys.* **50** 070101
[75] Simmons J G 1963 Generalized formula for the electric tunnel effect between similar electrodes separated by a thin insulating film *J. Appl. Phys.* **34** 1793
[76] Wang Q *et al* 2021 Efficient Ohmic contacts and built-in atomic sublayer protection in $MoSi_2N_4$ and WSi_2N_4 monolayers *npj 2D Mater. Appl.* **5** 71
[77] Shen P-C *et al* 2021 Ultralow contact resistance between semimetal and monolayer semiconductors *Nature* **593** 211